

Thermoplastic Elastomer Tunes Phase Structure and Promotes Stretchability of High-Efficiency Organic Solar Cells

Zhongxiang Peng, Kaihu Xian, Yong Cui, Qingchun Qi, Junwei Liu, Ye Xu, Yubo Chai, Chunming Yang, Jianhui Hou, Yanhou Geng, and Long Ye*

Top-performance organic solar cells (OSCs) consisting of conjugated polymer donors and nonfullerene small molecule acceptors (NF-SMAs) deliver rapid increases in efficiencies. Nevertheless, many of the polymer donors exhibit high stiffness and small molecule acceptors are very brittle, which limit their applications in wearable devices. Here, a simple and effective strategy is reported to improve the stretchability and reduce the stiffness of high-efficiency polymer:NF-SMA blends and simultaneously maintain the high efficiency by incorporating a low-cost commercial thermoplastic elastomer, polystyrene-*block*-poly(ethylene-*ran*-butylene)-*block*-polystyrene (SEBS). The microstructure, mechanical properties, and photovoltaic performance of PM6:N3 with varied SEBS contents and the molecular weight dependence of SEBS on microstructure and mechanical properties are thoroughly characterized. This strategy for mechanical performance improvement exhibits excellent applicability in some other OSC blend systems, e.g., PBQx-TF:eC9-2Cl and PBDB-T:ITIC. More crucially, the elastic modulus of such complex ternary blends can be nicely predicted by a mechanical model. Therefore, incorporating thermoplastic elastomers is a widely applicable and cost-effective strategy to improve mechanical properties of nonfullerene OSCs and beyond.

the power conversion efficiencies (PCEs) of OSCs show rapid increase and the values have increased to over 18%.^[16–24] However, owing to the brittle nature of small molecules,^[25] the mechanical properties of polymer:NF-SMA blends are generally insufficient and can hardly meet the requirement of stretchable electronics.^[26,27] The mechanical imperceptibility of OSCs requires low stiffness and high extensibility for wearable and portable applications. The human skin exhibits a ductility of about 30%, which is the benchmark for skin-wearable devices.^[28] Studies have been carried out to determine the mechanical properties of nonfullerene OSCs^[29–31] and drive the development of stretchable OSCs.^[32–35] For instance, the fracture strain of the well-known PTB7-Th:(3,9-bis(2-methylene-(3-(1,1-dicyanomethylene)-indanone))-5,5,11,11-tetrakis(4-hexylphenyl)-dithieno[2,3-d':3'-d'']-s-indaceno[1,2-b:5,6-b']dithiophene) (ITIC) blend films decreased dramatically

with the increase of ITIC, and the blend films became significantly stiffer as a result of increased elastic modulus.^[26,36] Therefore, methods should be adopted to improve the stretchability and reduce the stiffness of OSCs based on polymer:NF-SMA blends.


As the mechanical performance of polymer:NF-SMA blends are often poor, a representative high-efficiency

1. Introduction

Organic solar cells (OSCs) possess great potential for wearable/portable electronics and modern buildings owing to the merits of color tunability, semitransparency, and light weight.^[1–11] In recent years, thanks to the development of various nonfullerene small molecule acceptors (NF-SMAs),^[12–15]

Z. Peng, K. Xian, Q. Qi, J. Liu, Y. Chai, Y. Geng, L. Ye
 School of Materials Science and Engineering
 Tianjin Key Laboratory of Composite and Functional Materials
 Tianjin University
 Tianjin 300350, China
 E-mail: yelong@tju.edu.cn

Z. Peng, J. Liu, L. Ye
 State Key Laboratory of Applied Optics
 Changchun Institute of Optics
 Fine Mechanics and Physics
 Chinese Academy of Sciences
 Changchun 130033, China

 The ORCID identification number(s) for the author(s) of this article can be found under <https://doi.org/10.1002/adma.202106732>.

DOI: 10.1002/adma.202106732

Y. Cui, Y. Xu, J. Hou
 Beijing National Laboratory for Molecular Sciences
 State Key Laboratory of Polymer Physics and Chemistry
 CAS Research/Education Center for Excellence in Molecular Sciences
 Institute of Chemistry
 Chinese Academy of Sciences
 Beijing 100190, China

C. Yang
 Shanghai Synchrotron Radiation Facility
 Shanghai Advanced Research Institute
 Chinese Academy of Sciences
 Shanghai 201204, China

Y. Geng
 Joint School of National University of Singapore and Tianjin University
 International Campus of Tianjin University
 Binhai New City, Fuzhou 350207, China

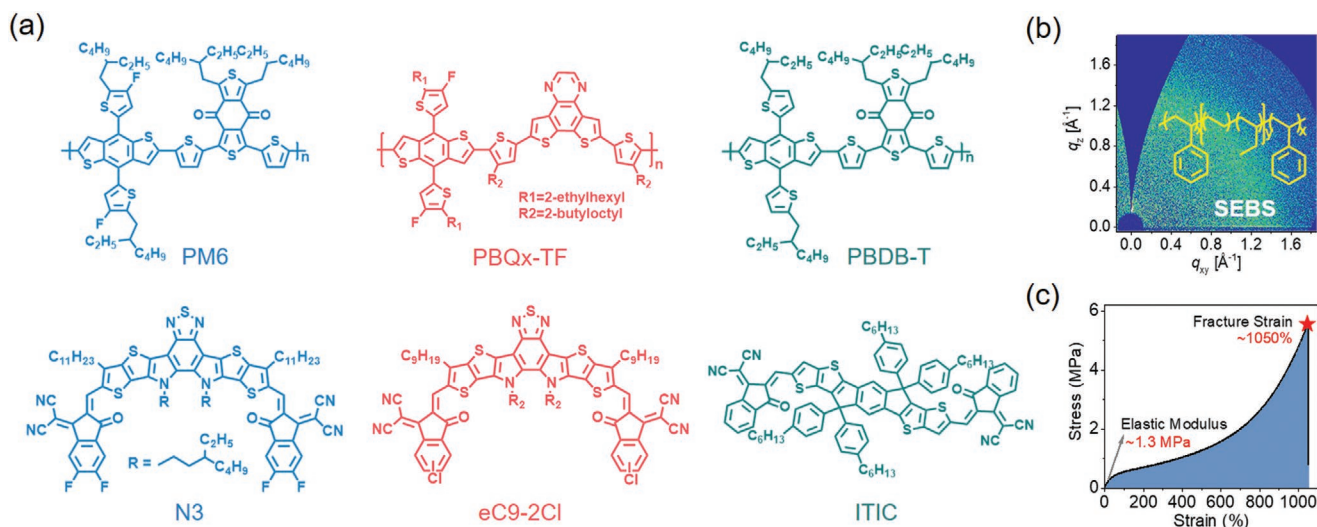


Figure 1. a) Molecular structures of the polymer donor and fullerene-free small molecular acceptor materials used in this work. b) 2D GIWAXS pattern of the neat thermoplastic elastomer film. Inset is the chemical structure of the thermoplastic elastomer SEBS. c) Stress–strain curve of bulk SEBS. The curve was measured at a tensile rate of 10 mm min^{−1} at room temperature. The elastic modulus and elongation at break are noted.

polymer:NF-SMA blend needs to be used as the primary system to initiate our study. A recently developed binary blend PM6: (2,2'-(2Z,2'Z)-((12,13-bis(3-ethylheptyl)-3,9-diundecyl-12,13-dihydro-[1,2,5]thiadiazolo[3,4-e]thieno[2'',3'':4'',5'']thieno[2'',3'':4'',5'']pyrrolo[3,2-g]thieno[2'',3'':4'',5'']thieno[3,2-b]indole-2,10-diyl)bis(methanylylidene))bis(5,6-difluoro-3-oxo-2,3-dihydro-1H-indene-2,1-diylidene))dimalononitrile) (N3)^[37] (the chemical structures are shown in Figure 1a) has received increasing attention in the research community. This blend system can harvest the photons in a very broad wavelength range of 300–1000 nm and has been used as the model photovoltaic system for various fundamental studies of nonfullerene OSCs.^[31,37–40] Recently, PM6:N3 based solar cells achieved a respectable efficiency of over 17.5% through meticulous device optimization.^[39] Nevertheless, this binary polymer:NF-SMA blend is quite brittle with the crack-onset strain (COS) is only ≈7% and stiff with an elastic modulus on the order of ≈1 GPa,^[31] both of which severely limit its application in stretchable electronics. It is thus quite desired to develop a simple method to boost the mechanical robustness of this high-efficiency system and its close variations.^[41–45]

To address these needs, we have successfully improved the stretchability and reduced the stiffness of the PM6:N3 blend film and simultaneously maintained its high efficiency by physically mixing this binary blend with a commercially accessible thermoplastic elastomer, polystyrene-*block*-poly(ethylene-*ran*-butylene)-*block*-polystyrene (SEBS), which exhibits isotropically disordered packing (Figure 1b). When a moderate weight amount (30%) of SEBS was added to the blend films, the COS of the films can be improved by a factor of ≈2 and the elastic modulus dropped to ≈1/4 of that without SEBS. The addition of small amount of (less than 5 wt%) SEBS could slightly improve the PCE values from ≈15.4% to ≈16%. As the content of SEBS further increased, the donor and acceptor in the active layer were diluted, resulting in a gradual decrease in the absorption coefficient and an increase in semi-transparency of blend films. In addition, the addition of SEBS also lead

to a minor improvement in PCE value for a high-efficiency polymer:nonfullerene PBQx-TF: (2,2'-(2Z,2'Z)-((12,13-bis(2-butylheptyl)-3,9-dinonyl-12,13-dihydro-[1,2,5]thiadiazolo[3,4-e]thieno[2'',3'':4'',5'']thieno[2'',3'':4'',5'']pyrrolo[3,2-g]thieno[2'',3'':4'',5'']thieno[3,2-b]indole-2,10-diyl)bis(methanylylidene))bis(6-chloro-3-oxo-2,3-dihydro-1H-indene-2,1-diylidene))dimalononitrile) (eC9-2Cl), which was most recently used to construct the nearly 19% efficiency ternary blend OSCs.^[46] More importantly, the elastic modulus of PM6:N3:SEBS blend films can be predicted by a classic mechanical model, i.e., Coran-Patel model. The strategy of applying SEBS to improve stretchability and reduce stiffness was also found to be very effective for PBQx-TF:eC9-2Cl and a benchmark polymer: nonfullerene PBDB-T:ITIC (the chemical structures are shown in Figure 1a); the modulus of the resultant blend films follows the same master curve of Coran-Patel model. Besides, the molecular weight effect of SEBS on the morphology and mechanical properties of the PM6:N3 blend film was explored. Therefore, adding thermoplastic elastomer is an efficient means to improve the stretchability and reduce the stiffness of polymer: small molecule blend and simultaneously preserve the high efficiency. We envision that introducing new types of elastomers will probably offer even better characteristics for versatile organic electronic systems (e.g., multifunctional organic photovoltaics and organic photodetectors).

2. Results and Discussion

2.1. Mechanical Properties of Ternary Blend Films

SEBS is a kind of commercial insulating thermoplastic elastomers with a very low cost of ≈0.005 \$ g^{−1}, which is approximately six orders of magnitude lower than that of the high-efficiency photovoltaic materials (about several thousand \$ g^{−1}, Table S1, Supporting Information). Owing to its soft nature and excellent aging resistance, SEBS has been widely used and can be easily accessible.^[47] Figure 1c presented the stress–strain curve

Table 1. Mechanical parameters of the PM6:N3 based blend films with varied SEBS contents measured by two methods.

SEBS content	FOE		AFM PFQNM
	Crack-onset strain [%]	Elastic modulus [GPa]	Elastic modulus [GPa]
0%	6.9 (± 0.4)	1.07 (± 0.04)	2.02 (± 0.03)
2%	8.1 (± 1.0)	0.98 (± 0.12)	1.78 (± 0.03)
5%	9.5 (± 0.5)	0.93 (± 0.10)	1.71 (± 0.04)
10%	11.2 (± 0.8)	0.77 (± 0.10)	1.62 (± 0.05)
20%	11.9 (± 0.4)	0.56 (± 0.08)	1.34 (± 0.02)
30%	13.0 (± 1.1)	0.28 (± 0.09)	1.01 (± 0.09)

The numbers in the parentheses are the standard deviations of over six samples for each blend.

of SEBS ($M_n = 153 \text{ kg mol}^{-1}$) primarily used in this research. The fracture strain is as high as $\approx 1050\%$ and two orders of magnitude higher than that of neat PM6, indicating that SEBS exhibits a remarkable ductility. The elastic modulus of SEBS is

determined to be 1.3 MPa, which is two to three orders of magnitude lower than those of common conjugated polymers.^[48,49] As seen from Figure S1a,b (Supporting Information), atomic force microscopy (AFM) characterizations showed that the neat SEBS film possesses a smooth surface and the root-mean-square roughness (R_q) is merely 0.68 nm. TEM characterizations (Figure S1c, Supporting Information) indicated that the bulk of neat SEBS films was pyknotic. The above physical properties render SEBS a promising third component for optimizing the phase structure and mechanical performance of our model polymer:NF-SMA blend.

To understand how the incorporation of SEBS affects the mechanical properties of PM6:N3 blend films, we mainly employed two methods, namely, film-on-elastomer (FOE)^[50–52] and peak force quantitative nanomechanical mapping (PFQNM) derived from AFM. The FOE method was used firstly and the obtained mechanical parameters and optical microscopy images of blend films were shown in Table 1, Figure 2a,b, and Figures S2 and S3 (Supporting Information). It can be seen that adding SEBS has a significant effect on improving stretchability and reducing stiffness. The COS of ternary blend films

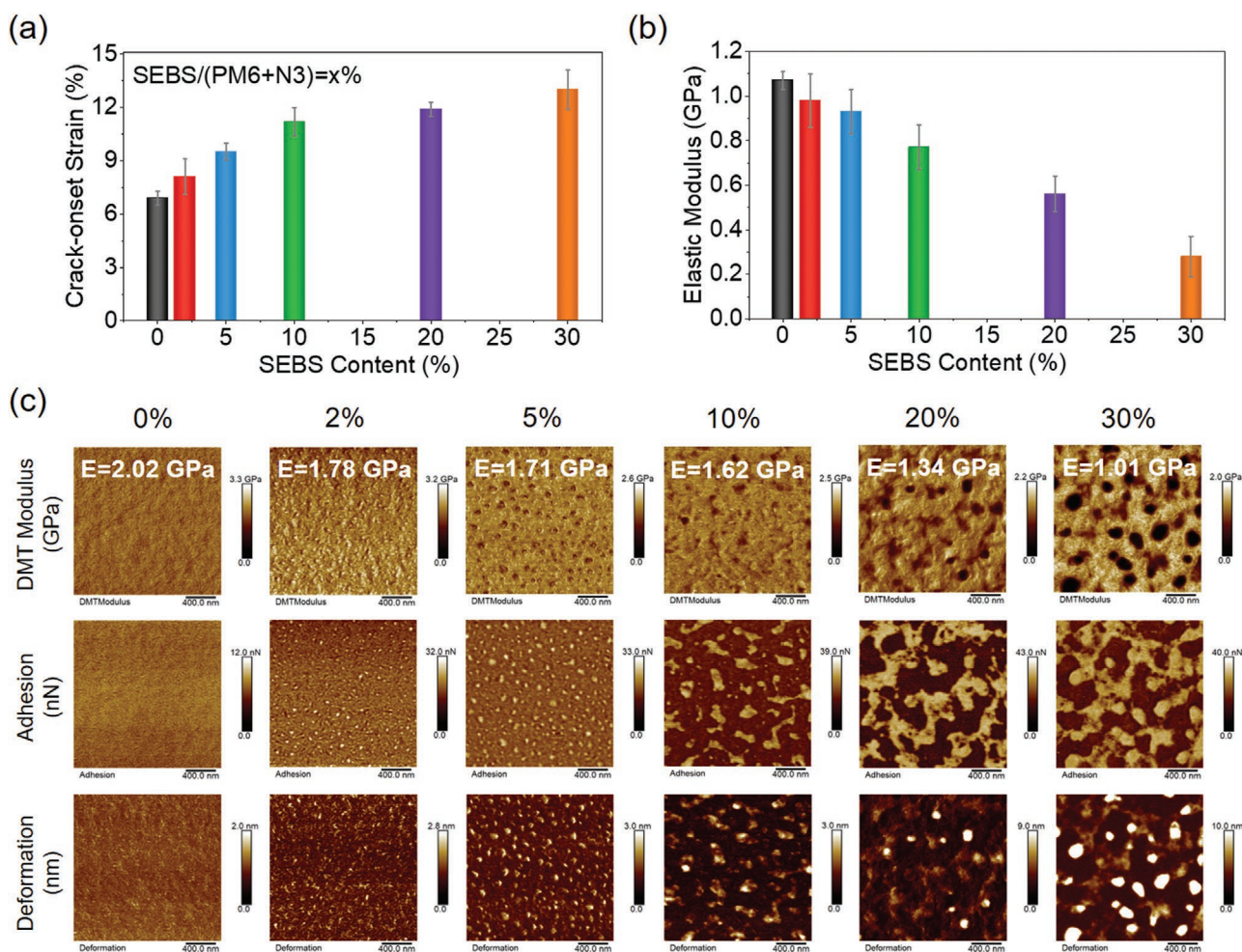


Figure 2. a) Crack-onset strain and b) elastic modulus of the PM6:N3:SEBS ternary blend films measured by FOE method. c) DMT modulus, adhesion, and deformation images of the PM6:N3:SEBS blend films with varying SEBS content obtained by the PFQNM method. The modulus data indicated in the DMT modulus images are average values. The scanned area is $2 \mu\text{m} \times 2 \mu\text{m}$.

gradually increased with the adding of SEBS. The average COS values of ternary blend films containing 2, 5, 10, 20, and 30 wt% SEBS were improved by 17%, 38%, 62%, 72%, and 88%, respectively, compared to that without SEBS. Meanwhile, the elastic modulus of ternary blend films monotonically decreased with the addition of SEBS. The modulus values were reduced by 8%, 13%, 28%, 48%, and 74% for the ternary blend films containing 2%, 5%, 10%, 20%, and 30% SEBS, respectively, compared to that without SEBS. Therefore, adding a moderate amount of SEBS (30%) in PM6:N3 could obtain a relatively high COS ($13.0 \pm 1.1\%$) and a relatively low modulus (0.28 ± 0.09 GPa). The improvement of mechanical properties can be attributed to the addition of the soft/ductile component SEBS and the optimization of the aggregate structure, which will be discussed later. Besides, the addition of SEBS could considerably reduce the crack size under high strain. As shown in Figure S4 (Supporting Information), the crack size of blend films under 30% strain showed a decreasing tendency with the augment of SEBS content.

To verify the variations of mechanical parameters obtained by the FOE method, PFQNM was also used to provide elastic modulus and additional morphology/mechanical information. PFQNM can obtain the quantitative nanomechanical properties of the material in addition to obtaining the morphology of the sample. Briefly, one needs to obtain the force curve first, and then perform fitting analysis and calculation on the force curve through the DMT model.^[53] This method has been effectively applied in measuring the modulus of the organic neat/blend films and investigating diffusion behaviors of fullerene into conjugated polymers.^[31,49,54,55] As shown in Figure 2c and Table 1, the elastic modulus decreased by 12%, 15%, 20%, 34%, and 50% with the addition of 2%, 5%, 10%, 20%, and 30% SEBS in ternary blend films, compared to that without SEBS. Although the modulus values achieved by PFQNM were slightly different from those obtained by FOE due to different characterization principles,^[44] the variation tendency was consistent. It is worth noting that some clear dark areas correspond to low modulus areas only in the modulus images of ternary blend films. The low modulus areas gradually darkened in color and gradually increased in size with the increase of the SEBS content. Hence, these low modulus areas were identified as SEBS domains, as the elastic modulus of SEBS is much lower than those of PM6 and N3.^[31] It is obvious that phase separation occurs between SEBS and PM6/N3, and SEBS tends to form self-aggregation. The darker color indicated the more enriched SEBS domain, while a larger size of the low modulus area suggested a larger size of the SEBS domain. However, the DMT modulus images alone cannot accurately reflect the SEBS domain distribution, and other information is needed.

Besides DMT modulus images, the adhesion and deformation images were also captured simultaneously. Through the analysis of adhesion and deformation images, we could obtain more morphological information. There are some bright areas in adhesion images (high adhesion areas) and in deformation images (high deformation areas) of ternary blend films. The size of those bright areas gradually increased, the values of adhesion and deformation of these areas showed an increasing trend with the augment of SEBS content. As SEBS has higher adhesion and deformation than PM6/N3 which attributes to the

soft characteristics of SEBS; meanwhile, the shape and size variation of these bright areas were consistent to a certain extent with the dark areas in the modulus images, the bright areas in adhesion and deformation images were also identified as SEBS domain. It should be pointed out that, combining the adhesion images and the deformation images, the SEBS domains were not simply distributed in the very dark (very small modulus) areas in the modulus images, but the areas with lower modulus in the images are all SEBS-rich domain, the areas with smaller modulus signified more enriched in SEBS. Hence, correlating the DMT modulus, adhesion and deformation images, we can clearly see the distribution of SEBS domain in blend films that SEBS formed quite isolated domains surrounding by the photo-active materials. More specifically, the shape variation of SEBS on the film surface can be inferred through adhesion images. When the SEBS content was low ($\leq 5\%$), the SEBS domains were spherical-like phases with a small size. When the content of SEBS was a bit higher ($\leq 10\%$), the SEBS domain turns to irregular, and when the content was much higher ($\geq 20\%$), the SEBS domain started to connect.

Additionally, film-on-water (FOW)^[56–58] was used to verify the variations of the tensile properties measured by FOE and PFQNM. The obtained stress–strain curves of PM6:N3 and PM6:N3:SEBS (30%) blend films (Figure S5, Supporting Information) showed that fracture strain increased and elastic modulus reduced with the addition of SEBS, which are consistent with FOE and PFQNM measurements. Therefore, it can be concluded that adding SEBS could improve the stretchability and reduce the stiffness of the blend film, and the SEBS domain can be observed intuitively via PFQNM characterization.

2.2. Film Morphology of Ternary Blend Films

To further confirm the phase structure of the images obtained by PFQNM, AFM tapping mode was employed to characterize the surface morphology of the ternary blend films. The AFM height and phase images were shown in Figure 3a. Evidently, the adding of SEBS can increase the surface roughness of the blend films. The R_q of blend films increased with the addition of SEBS, which attributes to the increase of SEBS aggregation. The simultaneously obtained phase images showed a similar morphology with the height images and the low degree areas correspond to the low height areas. Combining the adhesion and deformation images, the SEBS domain may not simply distribute in the very dark (height very low) areas of the height images, but also in other slightly lower areas, the areas with lower height signified more enriched in SEBS.

To complement the surface morphology results, we used TEM to visualize the bulk morphology of the blend films. As depicted in Figure 3b, there were only “fibers” in the PM6:N3 binary blend film, while there were some clear bright areas in the ternary blend film and the size of these areas increased with the augment of the SEBS content. According to the significant difference of chemical structure between SEBS and PM6/N3, and the previous images from PFQNM and AFM, we consider that the bright areas are SEBS domains.

To quantitatively attain the SEBS domain size and phase separation of blend films, the power spectral density (PSD)

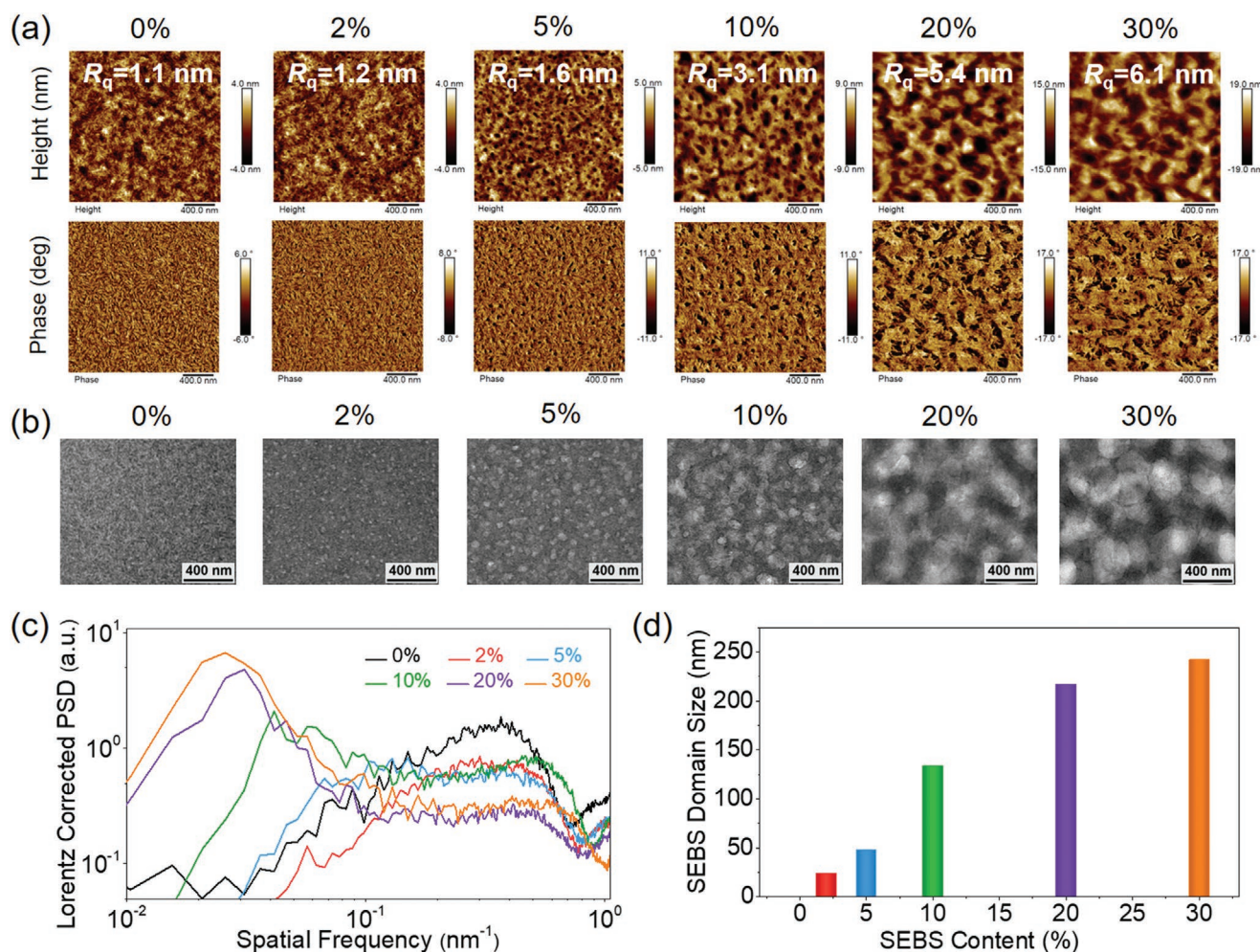


Figure 3. a) Height (top) and phase images (bottom) of the PM6:N3:SEBS blend films with varied SEBS content obtained by AFM tapping mode. The scanned area is $2\ \mu\text{m} \times 2\ \mu\text{m}$. b) TEM images of PM6:N3:SEBS blend films with varying SEBS content. c) Lorentz corrected PSD profiles of the TEM images. d) Plot of SEBS domain size with the SEBS content added to the PM6:N3 blend films.

profiles were obtained by Fourier transform analysis of the TEM images,^[59,60] as shown in Figure 3c. The PM6 and N3 phase separation of blend films with different SEBS contents remained similar and the domain sizes were all $\approx 17\ \text{nm}$. However, as seen from Figure 3d, the SEBS domain monotonically coarsened and the sizes were 24, 48, 134, 217, and 242 nm when 2%, 5%, 10%, 20%, and 30% SEBS content are used. Obviously, the variation tendency of the SEBS domain in film bulk was consistent with that in surface, despite their minor difference in values. The SEBS domains were isolated and spherical when SEBS content is very low ($\leq 5\%$), and then they became irregular-shaped and connected when SEBS content increased ($\geq 10\%$).

We further analyzed the morphologies of the PM6:N3:SEBS blend films with infrared scattering-type scanning near-field optical microscopy (IR s-SNOM) to identify the aggregates observed in the blend film. IR s-SNOM is a surface-sensitive scanning probe technology. The s-SNOM has been used in obtaining component distribution in all polymer and polymer: small molecule blend films and monitoring polymorphism and phase coexistence in small-molecule organic thin films.^[61–64]

IR s-SNOM at infrared frequencies provides both the spectral and spatial information at nanoscale.^[65,66] Near-field amplitude (reflectivity or absorption) image at a specific wavelength enables the direct examination of the staining-free chemical distribution of nanoscale polymers in blends. The infrared spectroscopy curves of PM6, N3, and SEBS neat films obtained by Fourier transform infrared (FTIR) spectrometer were shown in Figure S6 (Supporting Information). As one of the characteristic absorption peaks of SEBS, $1379\ \text{cm}^{-1}$ was selected as the specific wavelength for characterization. Figure 4 shows the images of topography, mechanical phase, optical amplitude of reflectivity, and optical phase of absorption. The topography and mechanical phase were similar to the height and phase images obtained by AFM. The light areas (high amplitude) in optical amplitude images of reflectivity and blue areas (low phase) in optical phase images of absorption were identified as SEBS domains. They showed a similar trend with PFQNM, AFM, and TEM images and further elucidated the SEBS domain distribution in the ternary blend films.

To figure out the phase separation of ternary blend films, we investigated the miscibility between the PM6, N3, and SEBS.

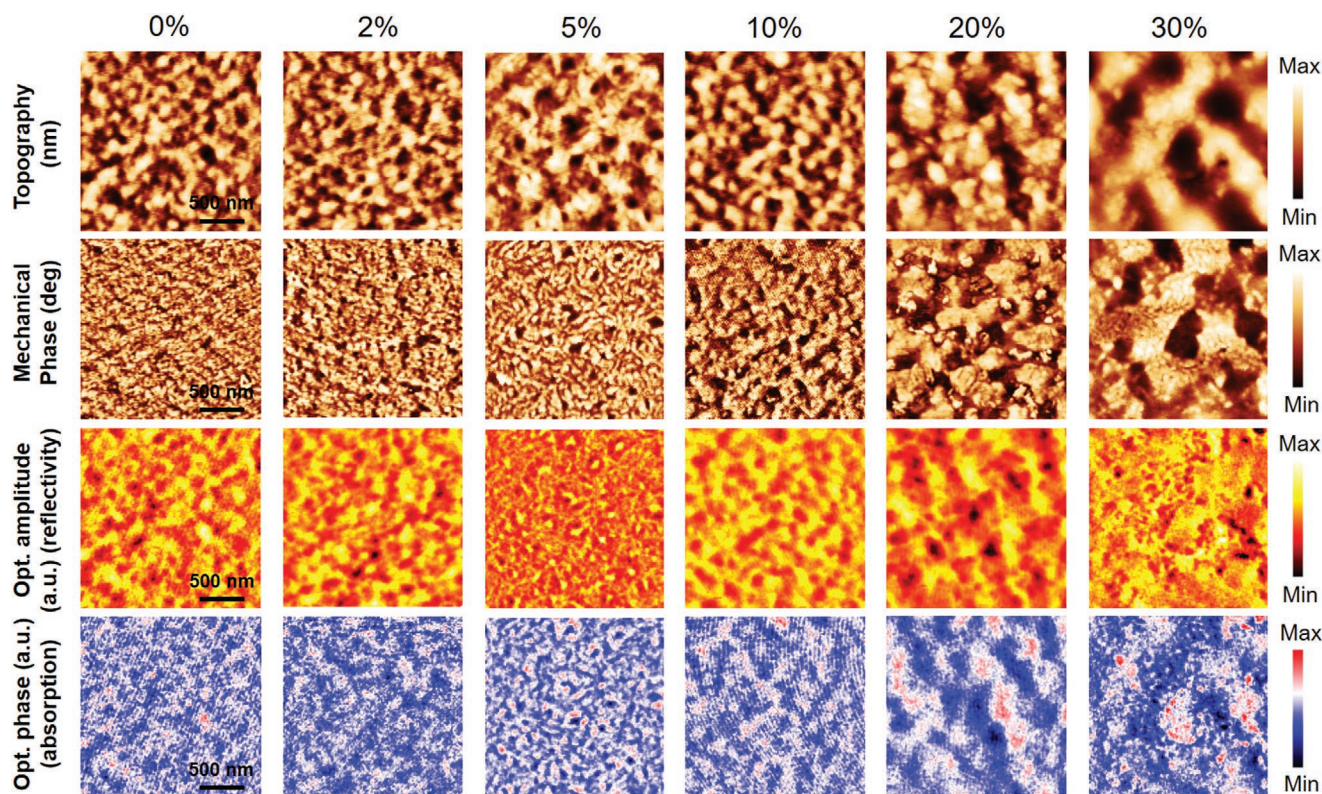


Figure 4. s-SNOM images of topography, mechanical phase, infrared optical amplitude (reflectivity), and optical amplitude (absorption) of the PM6:N3:SEBS blend films with varied SEBS contents at 1379 cm^{-1} . The scanned area is $2\text{ }\mu\text{m} \times 2\text{ }\mu\text{m}$.

The relative χ_{aa} parameters of materials were acquired via the contact angle measurements at room temperature. The water contact angle and ethylene glycol (EG) contact angle of PM6, N3, and SEBS neat films were measured to calculate the surface tension (γ) of the neat films. As shown in Table S2 and Figure S7 (Supporting Information). The γ of the PM6, N3, and SEBS were 23.72, 26.20, and 18.35 mN m^{-1} , respectively. The relative χ_{aa} of the materials can be calculated from an empirical equation: $\chi_{aa} = K(\sqrt{\gamma_1} - \sqrt{\gamma_2})^2$, where K is a positive constant (a typical value is $116 \times 10^3\text{ m}^{-0.5}$).^[67] The relative χ_{aa} values followed the order of PM6:N3 (0.06 K) < PM6:SEBS (0.34 K) < N3:SEBS (0.70 K). The much larger relative χ_{aa} values between SEBS and PM6 or N3 mean the poor compatibility between SEBS and PM6 or N3. The thermodynamic miscibility analysis thus explains why SEBS is prone to form self-aggregation and separate from PM6/N3.

To understand the effect of SEBS on the molecular packing and texture of ternary blend films, we performed grazing-incidence wide-angle X-ray scattering (GIWAXS) characterization and related analysis for blend films with different SEBS contents. As shown in Figure 5a–e, the scattering intensity of the out-of-plane (010) peak (characteristic of π – π packing) increased first and then decreased slightly with the augment of SEBS content. As shown in Figure 5f, the 1D profiles of out-of-plane and in-plane directions for the blend films with different SEBS contents were similar. For a quantitative comparison, the π – π stacking distances and coherence lengths of out-of-plane (010) peaks were obtained by the multiple peak fitting of the 1D profiles and calculation via Scherrer Equation. As shown in

Table S3 (Supporting Information), the q location of PM6 (010) diffraction peak was about $q_z = 1.71\text{ }\text{\AA}^{-1}$ and the corresponding distance of π – π packing reached $\approx 3.67\text{ }\text{\AA}$. The q location of N3 (010) diffraction peak was about $q_z = 1.75\text{--}1.76\text{ }\text{\AA}^{-1}$ and the corresponding distance of π – π packing reached $3.59\text{--}3.57\text{ }\text{\AA}$. As shown in Figure 5g and Table S3 (Supporting Information), when SEBS content was less than 5%, the PM6 and N3 π – π stacking distance and coherence length remained the same and the values were 12.0 and 33.3 \AA , respectively. When SEBS content was 10–30%, the PM6 π – π coherence length then decreased slightly, and the values were 11.8 and 11.5 \AA for 10% and 30% SEBS, respectively. The π – π coherence length of N3 decreased a little bit and then remained unchanged, the values were 31.4 \AA (10–30%). To understand the molecular orientation of the blend films, the pole figure was extracted from the analysis by the (010) diffraction peaks of 2D patterns (shown in Figure 5h). Based on a detailed analysis of the pole figure, we extracted three important parameters, i.e., face-on fraction, edge-on fraction and isotropic fraction. As shown in Figure 5i and Table S4 (Supporting Information), face-on fraction first increased a little bit and then decreased gradually and slightly while edge-on fraction decreased first and increased subsequently with the augment of SEBS content. The face-on fractions of the blend films with different SEBS content were 41.0%, 45.2%, 41.4%, 40.1%, and 38.9% for the SEBS content increased from 0% to 30%, respectively. Therefore, it is clear that the addition of SEBS had little effect on the order of PM6/N3, but mainly affected the molecular orientation. The GIWAXS 2D patterns and diffractogram profiles along with the OOP and IP directions obtained

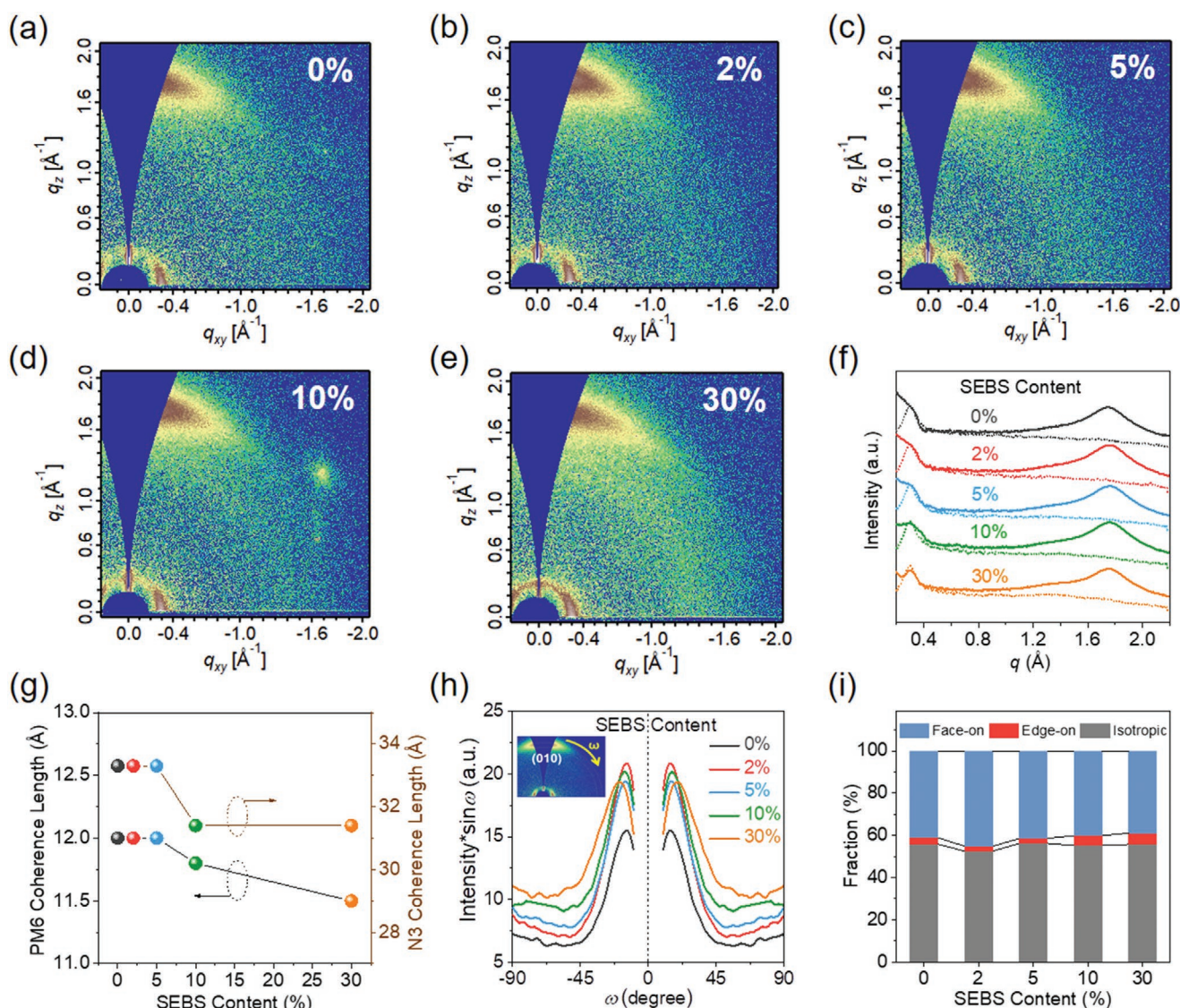


Figure 5. a–e) GIWAXS 2D patterns of the PM6:N3:SEBS blend films with varied SEBS contents. f) The corresponding GIWAXS diffractogram profiles along the out-of-plane (OOP) and in-plane (IP) directions. Solid lines and dashed lines represent OOP profiles and IP profiles, respectively. Data were shifted in the y -axis for clarity. g) PM6 and N3 π – π coherence length obtained by the analysis of OOP (010) peak. h) Pole figures extracted from the (010) diffraction of 2D GIWAXS patterns. ω is the (010) polar angle, as depicted in the inset image. i) The histogram of face-on/edge-on/isotropic fractions of blend films with SEBS content.

from a different beamline (Figure S8, Supporting Information) demonstrated a similar observation.

2.3. Photovoltaic Properties of Blend Films

To understand how the addition of SEBS affects the photovoltaic properties, we fabricated OSCs devices based on the conventional configuration of ITO/PEDOT:PSS/PM6:N3:SEBS/PFN-Br/Ag (Figure 6a). As shown in Figure 6b,c and Table 2, the average PCE, J_{sc} , and FF of blend devices increased firstly and then gradually decreased with the augment of SEBS, and reached the maximum value by merging 2% SEBS. Compared with the blend devices without SEBS (15.42%), the blend

devices with 2% SEBS showed an improved PCE of $\approx 16\%$, and the devices with 5% SEBS showed a similar PCE of 15.57%. When the SEBS content is up to and more than 10%, the PCEs of blend devices started to decrease and the maximum values reached 14.42% (10% SEBS), 13.10% (20% SEBS), and 11.55% (30% SEBS), which maintained 94%, 85%, and 75% compared with the binary devices (0%). In addition, the variation trend of the average J_{sc} of blend devices was similar to that of PCE. The J_{sc} variation may be related to charge mobility and the active layer light absorption. The electron and hole mobilities of blend films were investigated by the space-charge limited current (SCLC) model and the device configuration of ITO/ZnO/active layer/Al for electron-only devices and ITO/PEDOT:PSS/active layer/Au for hole-only devices. As shown in Figure S9

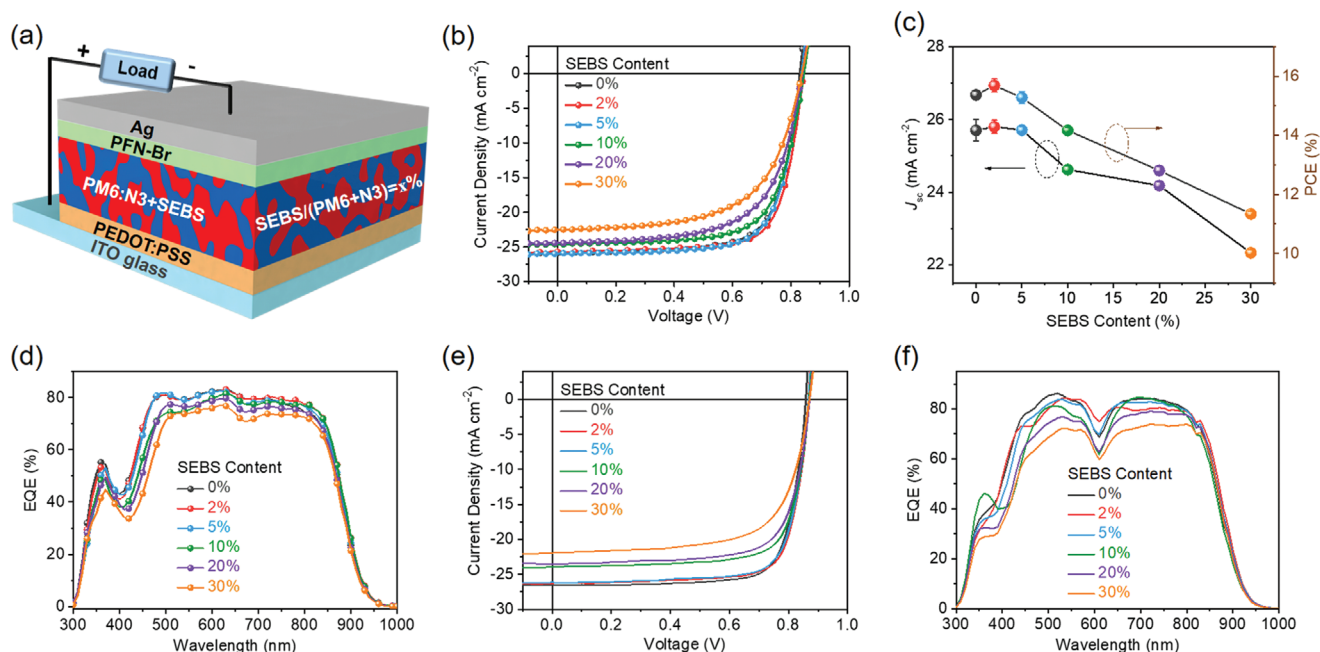


Figure 6. a) Conventional configuration of the ternary OSCs based on PM6:N3:SEBS blends. Here, x% is the weight ratio of SEBS compared to (PM6+N3) and the values here are 0–30%. b) Typical current density–voltage characteristics of the ternary OSCs under the optimized conditions based on PM6:N3:SEBS blends. c) The average J_{sc} and PCE plots as a function of SEBS content based on PM6:N3:SEBS blends. d) The EQE curves of the devices with various SEBS contents based on PM6:N3:SEBS blends. e) Typical current density–voltage characteristics of the ternary OSCs under the optimized conditions based on PBQx-TF:eC9-2Cl:SEBS blends. f) The EQE curves of the devices with various SEBS contents based on PBQx-TF:eC9-2Cl:SEBS blends.

and Table S5 (Supporting Information), electron mobility (μ_e) increased firstly and then decreased while hole mobility (μ_h) decreased monotonically with the augment of SEBS content. Therefore, the values of μ_e/μ_h increased first and subsequently decreased. The addition of SEBS may not conducive to the transportation of holes but a benefit for electron transportation. In addition, as shown in Figure S10 (Supporting Information), the UV–visible absorption coefficient of ternary blend films gradually reduced with the addition of SEBS, which can be understood by the absorption spectra of SEBS (Figure S11, Supporting Information). As the thicknesses are quite similar (110 nm), the film with high SEBS contents possesses lower material cost and higher transparency. Moreover, the FF of blend devices showed a similar variation trend with PCE and J_{sc} and the average FF values were increased from 71.7% (0% SEBS) to 72.4% (2% SEBS) and then reduced to 60.5%

(30% SEBS). Therefore, the variation of PCE was mainly related to J_{sc} and FF. The J_{sc} value was verified by external quantum efficiency (EQE) measurements and the values agreed well with the measured J_{sc} with an acceptable mismatch within 5% (Figure 6d and Table 2). To verify the effect of SEBS on the photovoltaic performance of high-efficiency blend system, the OSC devices based on PBQx-TF:eC9-2Cl:SEBS with varied SEBS contents were also prepared and measured. PBQx-TF:eC9-2Cl was a recently emerged system that constructs the present record-efficiency single-junction ternary blend OSCs and the binary itself produced an impressive efficiency of over 17%.^[41] As shown in Figure 6e and Table S6 (Supporting Information), the PCE of PBQx-TF:eC9-2Cl blend slightly increased from 17.72% to 17.84% by adding 2% SEBS. The PCE of the OSC device with 5% SEBS can achieve a decent PCE value of 17.54%. As the addition of SEBS continues to increase, PCE gradually

Table 2. Photovoltaic characteristics of the best-performing photovoltaic devices based on the PM6:N3 blend films with various SEBS content, under the illumination of AM 1.5G 100 mW cm^{−2}.

SEBS content	$V_{oc}^{a)}$ [mV]	J_{sc} [mA cm ^{−2}]	$J_{cal}^{b)}$ [mA cm ^{−2}]	FF [%]	PCE [%]
0%	834 ± 4 (830)	25.70 ± 0.30 (25.87)	24.71	71.7 ± 0.5 (71.8)	15.37 ± 0.14 (15.42)
2%	839 ± 3 (843)	25.80 ± 0.18 (25.69)	25.04	72.4 ± 1.0 (73.8)	15.69 ± 0.22 (15.98)
5%	839 ± 3 (836)	25.71 ± 0.10 (25.94)	24.65	70.9 ± 0.7 (71.8)	15.28 ± 0.20 (15.57)
10%	839 ± 2 (845)	24.62 ± 0.10 (24.59)	24.00	68.6 ± 0.3 (69.4)	14.17 ± 0.11 (14.42)
20%	840 ± 2 (839)	24.18 ± 0.12 (24.43)	23.36	63.1 ± 0.5 (63.9)	12.81 ± 0.15 (13.10)
30%	839 ± 3 (838)	22.33 ± 0.08 (22.48)	22.23	60.5 ± 0.4 (61.3)	11.34 ± 0.09 (11.55)

^{a)}Statistical results are obtained from over 15 devices. The maximum results are listed in the parentheses; ^{b)}Current densities calculated from EQE data.

decreased. The reduced PCE was mainly related to reduced J_{sc} and reduced FF. The J_{sc} values were also verified by EQE measurements and the values agreed well with the measured J_{sc} with an acceptable mismatch within 5% (Figure 6f and Table S6, Supporting Information). Hence, SEBS plays a similar role in the polymer:NF-SMA blend system, that is, PCE increases slightly at first, and then gradually decreases slowly.

2.4. Elastic Modulus Prediction

To understand and predict the elastic modulus of blend films, theoretical equations should be used. The Voigt model (parallel model) and Reuss model (series model) are common mechanical models, which generally represent the upper bound and lower bound of the elastic modulus of composites.^[68–72] Besides, Coran-Patel model is an empirical formula for predicting the elastic modulus of heterogeneous polymer composites,^[69,72] which is derived from the phenomenological adjustment on Voigt model and Reuss model. The full expression of Coran-Patel model is as follows

$$E_c = \phi_h^n (n\phi_s + 1)(E_u - E_l) + E_l \quad (1)$$

where E_c is the elastic modulus of composite, ϕ_h and ϕ_s are the volume fraction of the hard phase and soft phase, respectively. n is an adjustable parameter, which can be inferred from the known modulus of pure component and at least one modulus of the blend composite. Once n can be determined, the modulus of the blend system can be predicted through the Coran-Patel model. The higher n value means that the blend is much softer. E_u and E_l are the upper-bound modulus and lower-bound modulus of the composite, respectively, and they are given by

$$E_u = E_h\phi_h + E_s\phi_s \quad (2)$$

$$E_l = \frac{E_s E_h}{\phi_h E_s + \phi_s E_h} \quad (3)$$

where E_h and E_s are the elastic modulus of the pure hard phase and pure soft phase, respectively. Here, PM6:N3 is simplified as a mixed phase (hard polymer domain) and SEBS is considered a soft phase (soft polymer domain). The volume fractions of the phases are estimated based on a typical mass density of 1.12, 1.2, and 0.89 g cm^{−3} for PM6, N3, and SEBS, respectively. The n parameter is determined to be 6 in our prediction for this blend system. As shown in Figure 7a, the experimental data of the modulus of the blend films measured by FOE method are quite close to the predicted values from Coran-Patel model and are located between the Voigt model and Reuss model. Despite the simplification, this Coran-Patel model perfectly fits the elastic modulus of the PM6:N3:SEBS ternary blends. In addition, this Coran-Patel model appears to be a feasible model for predicting the modulus of ternary systems based on dual polymers, for example, blends based on two polymer donors and one small molecule acceptor.

To verify the applicability of SEBS for improving the mechanical robustness for other polymer:nonfullerene small molecule systems, we selected a novel combination PBQx-TF:eC9-2Cl

and a benchmark blend PBDB-T:ITIC as two additional active layer systems. Similarly, FOE and PFQNM were used to characterize the mechanical parameters of the films. The COS and elastic modulus values of neat PBQx-TF and eC9-2Cl films were investigated and the results were shown in Table S7 and Figures S12 and S13 (Supporting Information). The COS values of PBQx-TF and eC9-2Cl were all small (<6%) and eC9-2Cl was much more brittle than PBQx-TF (<2%). In addition, eC9-2Cl showed more stiffness than PBQx-TF, as can be seen from that eC9-2Cl has higher modulus. As shown in Figure 7b, Table S8 and Figure S14 (Supporting Information), the COS of PBQx-TF:eC9-2Cl:SEBS blend films substantially increased with the addition of SEBS and the values were improved by 5%, 16%, 32%, 49%, and 108% for 2–30% SEBS contents, respectively, compared to that of PBQx-TF:eC9-2Cl binary blend. Meanwhile, as shown in Table S8 and Figure S15 (Supporting Information), the modulus of PBQx-TF:eC9-2Cl:SEBS blend films significantly decreased with the addition of SEBS and the values showed the reduction by 5%, 19%, and 33% for 2–10% SEBS content, respectively, compared to that without SEBS. As the modulus of the blend films containing 20% and 30% SEBS are too small to produce wrinkles, the elastic modulus cannot be calculated by the FOE method. Therefore, PFQNM was used to provide full elastic modulus and additional mechanical information of blend films for verifying the variations of elastic modulus obtained by the FOE method. As shown in Figure 7c and Figure S16 (Supporting Information), the elastic modulus measured by PFQNM showed the same variation with the FOE method that modulus monotonically decreased with the augment of SEBS content. The modulus of PBQx-TF:eC9-2Cl:SEBS blend films significantly decreased with the addition of SEBS and the values showed the reduction by 10%, 17%, 27%, 54%, and 62% for 2–30% SEBS content, respectively, compared to that without SEBS. In addition, it can be observed that there were “low modulus areas” in adhesion images, “high deformation areas” in deformation images of PBQx-TF:eC9-2Cl:SEBS blend films, similar to the PM6:N3:SEBS blend films. The low modulus areas became larger and darker with the adding of SEBS. Considering the intrinsic properties of SEBS (low modulus), these areas were also recognized as SEBS-rich areas. Hence, this proves that SEBS tends to form quite isolated domains surrounding the photoactive materials. As shown in Figure 7d, the modulus values can also be predicted by the Coran-Patel model. It can be seen that the experimental data were all close to the master curve of the Coran-Patel model and distributed between the two basic models (i.e., Voigt model and Reuss model). In addition, as shown in Figure S17 (Supporting Information), the crack size of PBQx-TF:eC9-2Cl:SEBS blend films showed a reducing tendency with the addition of SEBS. Therefore, it is clear that SEBS can also promote the stretchability and reduce the stiffness of PBQx-TF:eC9-2Cl blend films. Adding SEBS is a very effective strategy to enhance the stretchability and reduce the stiffness of these most recent record system polymer:nonfullerene blend films as well.

The PBDB-T:ITIC based OSCs significantly outperformed fullerene-based OSCs for the first time in 2016 and received worldwide attention.^[73] The mechanical parameters of neat PBDB-T and ITIC films were investigated and the results were

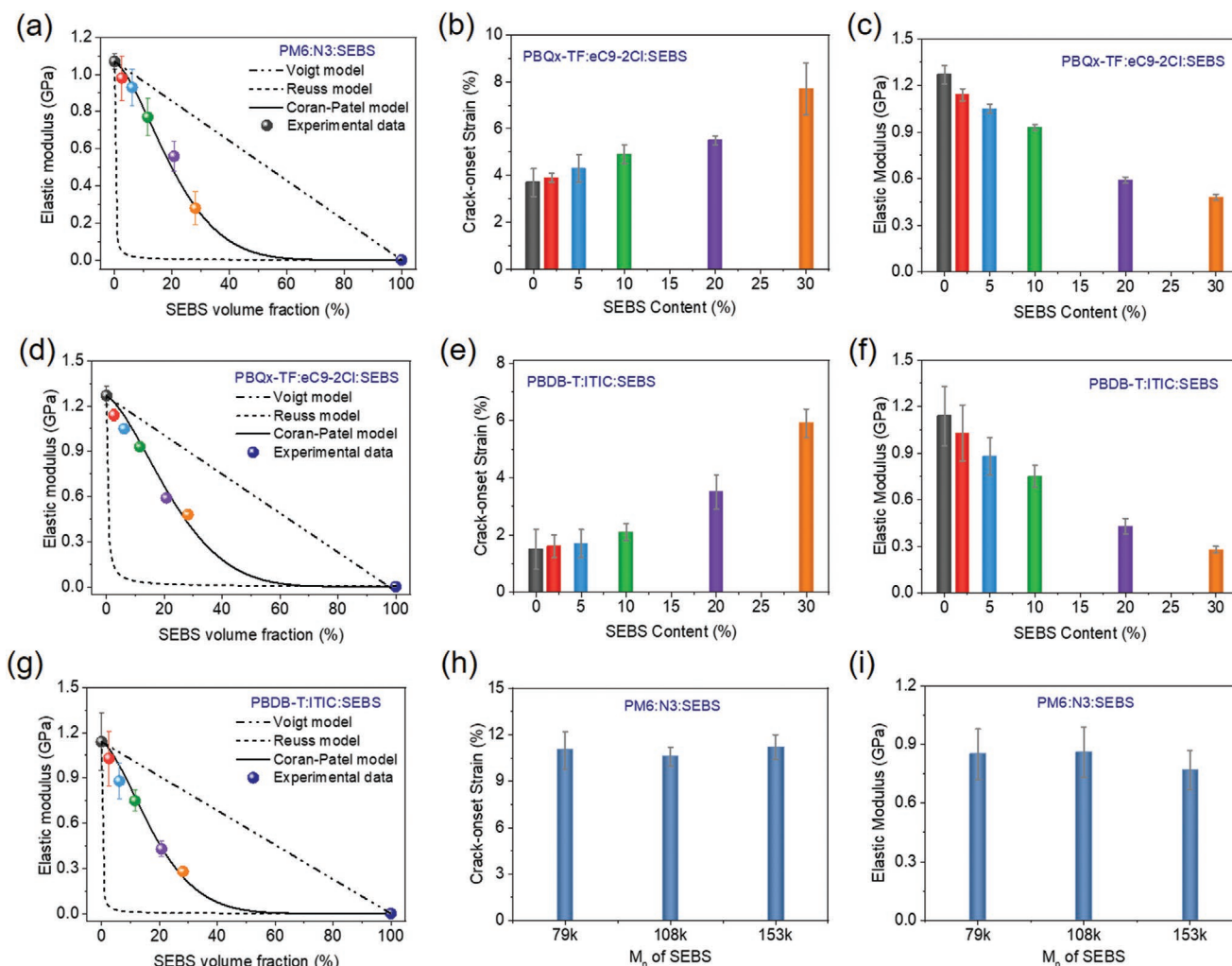


Figure 7. a) Theoretical prediction with three models and experimental elastic modulus data of PM6:N3:SEBS blend films obtained by the FOE method. b) The crack-onset strain and c) elastic modulus of PBQx-TF:eC9-2Cl:SEBS ternary blend films obtained by the FOE and PFQNM methods. d) Theoretical prediction with three models and experimental elastic modulus data of PBQx-TF:eC9-2Cl:SEBS blend films. e) The crack-onset strain and f) elastic modulus of PBDB-T:ITIC:SEBS blend films obtained by the FOE method. g) Theoretical prediction with three models and experimental elastic modulus data of PBDB-T:ITIC:SEBS blend films. h) The crack-onset strain and i) elastic modulus of PM6:N3:SEBS (10%) ternary blend films with SEBS of different M_n obtained by the FOE method.

shown in Table S9 and Figure S18 (Supporting Information). The COS and elastic modulus of neat PBDB-T films were $8.1 \pm 0.6\%$ and 0.74 ± 0.05 GPa, respectively. In contrast, ITIC is much more brittle and stiffer, and the corresponding COS and modulus of neat ITIC films were $<1\%$ and 1.89 ± 0.32 GPa, respectively. As shown in Figure 7e, Table S10 and Figure S19 (Supporting Information), the COS of PBDB-T:ITIC:SEBS blend films substantially increased with the addition of SEBS and the values were improved by 7%, 13%, 40%, 133%, and 293% for 2–30% SEBS content, respectively, compared to that of PBDB-T:ITIC binary blend. Meanwhile, as shown in Figure 7f, Table S10 and Figure S20 (Supporting Information), the modulus of PBDB-T:ITIC:SEBS blend films significantly decreased with the addition of SEBS and the values showed the reduction by 10%, 23%, 34%, 62%, and 75% for 2–30% SEBS content, respectively, compared to that without SEBS. As shown in Figure 7g, the modulus values can also be understood by the

Coran-Patel model. In addition, as shown in Figure S21 (Supporting Information), the crack size of PBDB-T:ITIC:SEBS blend films also showed a reducing tendency with the addition of SEBS. Therefore, it is clear that SEBS can also promote the stretchability and reduce the stiffness of PBDB-T:ITIC blend films. To verify the variations of elastic modulus obtained by the FOE method, PFQNM was also used to provide elastic modulus and additional mechanical information. As shown in Figure S22 (Supporting Information), the elastic modulus of PBDB-T:ITIC:SEBS blend films measured by PFQNM showed the same variation with the FOE method that modulus monotonically decreased with the augment of SEBS content. The elastic modulus of blend films with 30% SEBS was 0.49 GPa, which is about $\approx 1/3$ of that without SEBS (1.37 GPa). In addition, the surface morphology was measured by AFM and shown in Figure S23 (Supporting Information). The R_q of blend films increased with the augment of SEBS content. The aggregates

in height images (bright areas) are also identified as SEBS domains and the size of the SEBS aggregates increased with the addition of SEBS. Therefore, adding SEBS is a very effective strategy to enhance the stretchability and reduce the stiffness of these benchmark polymer:nonfullerene small molecule blend films as well.

Considering that the molecular weight of the polymer affects the phase structure and mechanical properties of organic electronic blends,^[26,74] we also explored the impact of SEBS molecular weight on the mechanical properties, surface morphology, and bulk phase separation of PM6:N3:SEBS (10%) blend films with three different molecular weights of SEBS. As shown in Figure S24 (Supporting Information), the number-average molecular weight (M_n) of SEBS were 79, 108, and 153 kg mol⁻¹, which were labeled as 79k, 108k, and 153k, respectively. The mechanical properties of their blend films were obtained by FOE, and the results were shown in Figure 7h–i, Table S11 and Figures S25 and S26 (Supporting Information). All SEBS with different M_n can increase the ductility and reduce the stiffness of PM6:N3 blend films. The blend films with 153k SEBS exhibited a slightly higher COS and lower elastic modulus than that with 79k and 108k SEBS, but the difference of values was small. In addition, the elastic modulus and additional information of blend films were also obtained by PFQNM (Figure S27, Supporting Information), and the results showed that all SEBS with different M_n formed self-aggregated and isolated phases. The elastic modulus of blend films increased a bit with the higher M_n of SEBS, which is attributed to the amount of SEBS aggregation in the surface was a little different from that in bulk. The surface morphology and bulk separation were obtained by AFM and TEM, and the results are shown in Figure S28 (Supporting Information). The roughness of blend films showed a little increase with the higher M_n of SEBS. In addition, the size of SEBS domains in blend films was similar to that of different M_n of SEBS. Therefore, our results showed that the blend films with higher molecular-weight SEBS have slightly higher COS, lower modulus, and similar phase separation compared to the counterparts.

2.5. Correlations between Morphology and Mechanical/Photovoltaic Properties

The above results motivated us to think deeply about the relationship between morphology and mechanical/photovoltaic performance of this novel ternary system comprised of a polymer, a nonfullerene acceptor, and a thermoplastic elastomer. The full morphology-performance picture is demonstrated in Figure 8. Considering the soft/ductile properties of SEBS and the positive correlation between COS and SEBS domain size (Figure S29, Supporting Information), the deformation of SEBS and the size, shape, and distribution of SEBS in the ternary blend films play a critical role in mechanical stretching. Besides, the variation of PM6/N3 aggregate structure induced by adding SEBS may also affect the stretchable properties. When the SEBS content is low ($\approx 2\%$), the SEBS phase is isolated and small, which contribute to the improvement of stretchability for three reasons: more soft/ductile aid (small SEBS phases), better out-of-plane π - π stacking, and higher face-on fraction.^[31,75,76]

The increased π - π stacking and face-on population of PM6/N3 may play a major role. When the SEBS content is increased to 5%, the improvement of stretchability can be ascribed to the increase of soft/ductile component (SEBS) and more out-of-plane π - π stacking. When SEBS content is greater than 10 wt%, the improvement of stretchability can be mainly contributed to the addition of SEBS. At this point, the SEBS domain is already large and interconnected. SEBS in the blend films can prevent the chain-sliding effect of polymer donor/small molecule acceptor.

The photovoltaic performance of PM6:N3:SEBS blend films increased firstly and then decreased with the weight content of SEBS. For the weight contents of $<2\%$, the improved PCE and J_{sc} were attributed to the more out-of-plane π - π stacking and higher face-on population. On the basis of the improved μ_e and reduced μ_h , the more out-of-plane π - π stacking and higher face-on population can be attributed to the packing of N3 molecules. As the SEBS content is increased to 5%, similar PCE and J_{sc} were achieved. This is the combined result of the more out-of-plane π - π stacking, similar face-on population and negative effects of SEBS on PM6 stacking (reduced hole transport). When the SEBS content is up to 10%, the fraction of conjugated molecules became less ($\approx 91\%$ in the whole blend) and the size of the SEBS domain (≈ 134 nm) exceeds the thickness of the whole blend film (≈ 110 nm), which causes the drop of photon harvest area/volume. Therefore, these result in reduced PCE and J_{sc} . When the SEBS content is much higher ($>10\%$), the amount of harvested photon decreased, which causes much lower PCE and J_{sc} . As a consequence, the desired range of SEBS content for balancing stretchability and photovoltaic performance is 5–10% in PM6:N3:SEBS blend films. When the SEBS content is 5%, the photovoltaic performance is slightly improved, the COS increases by 38%, and the elastic modulus decreases by 13%. For the bend film with a SEBS content of 10%, the photovoltaic performance is almost unchanged, the COS increases by 62%, and the elastic modulus decreases by 28%. Above all, introducing both contents of SEBS are good recipes for targeting more appealing OSC active layers.

3. Conclusions

In summary, aiming at enhancing the stretchability and reducing the stiffness of high-efficiency polymer:nonfullerene blend systems while having a minor influence on their device operation, we have successfully employed a commercially available thermoplastic elastomer SEBS in the blends. Using PM6:N3 as a primary system of interest, we have thoroughly characterized the mechanical properties, surface morphology, bulk phase structure, molecular order, and photovoltaic performance of the blend films with varied SEBS contents. In the resultant PM6:N3:SEBS blend film, the COS increased gradually with the increase of SEBS weight content, while the modulus and crack size under the stretch of a certain strain (30%) monotonically decreases. Our scattering and microscopic characterizations suggest that adding a small weight amount of SEBS can improve the out-of-plane π - π stacking and face-on fraction meanwhile have little effect on the PM6/N3 phase

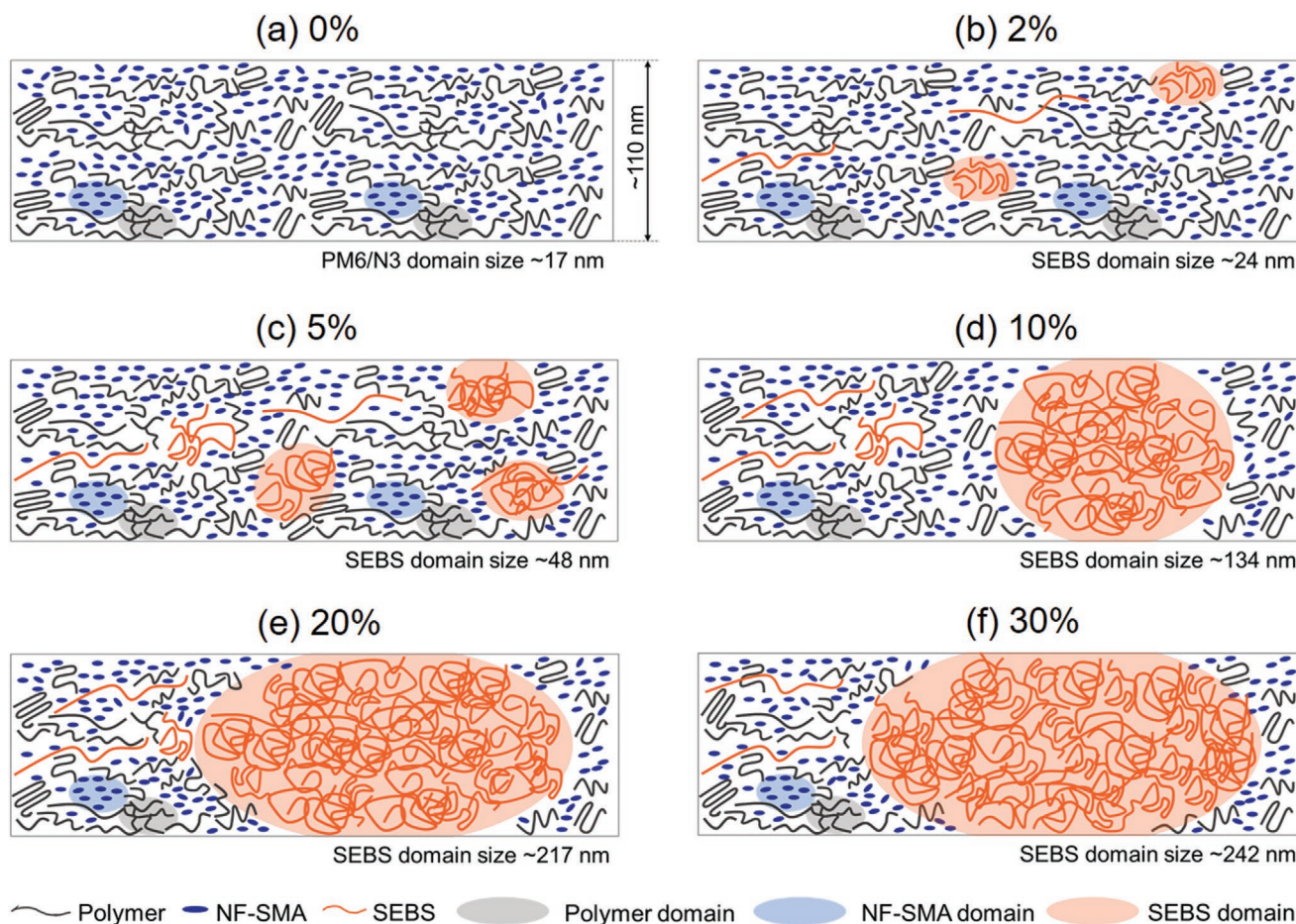


Figure 8. a–f) Schematic illustrating the role of SEBS in the morphology of polymer:NF-SMA:SEBS blend films with varied SEBS contents (0–30%). The schematic for each content was based on the microstructural data of PM6:N3:SEBS.

separation. As a consequence, the photovoltaic performance of ternary devices can be improved or remain similar at a small content (2–10%), compared to the binary devices.

Furthermore, the PBQx-TF:eC9-2Cl blend for constructing the nearly 19% efficiency single-junction OSCs was used as the second system. Similar PCE variation, improvement in COS, reduction in modulus and decrease in crack size under 30% strain were observed. Besides, the world-widely used PBDB-T:ITIC blend was used as the third system and similar mechanical improvements were observed. We also found that the molecular weight of SEBS has a minor influence on these ternary blends and the higher molecular weight elastomer gives rise to a slightly higher stretchability. More importantly, we verified that the elastic modulus of all three blend films (i.e., PM6:N3:SEBS, PBQx-TF:eC9-2Cl:SEBS, and PBDB-T:ITIC:SEBS) can be nicely modeled with a master curve derived from classic polymer mechanics, which enables the prediction of elastic modulus of complex blend films based on organic photovoltaic materials and polymer elastomers. In addition, due to the addition of a transparent component (SEBS), the diluted active layer yields an additional benefit, superior semi-transparency compared to the reference donor:acceptor blend. This work indicates that the addition of thermoplastic elastomer may be a widely applicable and cost-effective strategy to improve the stretchability

of nonfullerene OSCs and beyond.^[77] Undoubtedly, emerging polymer elastomers with distinct chemical structures deserve further exploration.

4. Experimental Section

Device Fabrication and Characterizations: The organic photovoltaic devices based on PM6:N3 were fabricated with a conventional architecture of ITO/PEDOT:PSS/active layer/PFN-Br/Ag. The PEDOT:PSS (Baytron PVP A14083) was spin-coated on the ITO glass at 4000 rpm for 30 s after the ITO glass was exposed by UV-ozone for 30 min. Then, PEDOT:PSS films were dried at 140 °C for 18 min by baking oven. The PM6:N3:SEBS blends with different weight SEBS content were dissolved in chloroform with different concentrations (the concentration of PM6 is 5–7 mg mL⁻¹) and adding 0.5% 1-chloronaphthalene (CN) as additive. The solutions were stirred at 45 °C for 2 h and then spin-coated on PEDOT:PSS layer at 2000–4000 rpm for 60 s to obtain the films with a thickness of ~110 nm. Then the active layers were annealed at 90 °C for 5 min. The PFN-Br solution was dissolved in methanol by being stirred overnight and then spin-coated on the active layer at 3000 rpm for 40 s. Finally, Ag was deposited as cathode through vacuum evaporation. The area of each device is 4 mm². The organic photovoltaic devices based on PBQx-TF:eC9-2Cl were fabricated with a conventional architecture of ITO/PEDOT:PSS/active layer/PFN-Br/Ag. The PBQx-TF:eC9-2Cl:SEBS blends with different weight SEBS content were dissolved in toluene (the concentration of PBQx-TF is 5–7 mg mL⁻¹) and adding 0.5%

1,8-diiodooctane (DIO) as additive. The solutions were stirred at 70 °C over 2 h and then spin-coated on PEDOT:PSS layer at 1500–4000 rpm for 60 s to obtain the films with a thickness of ≈ 100 nm. Then the active layers were annealed at 100 °C for 10 min. The PF3N-Br solution was dissolved in methanol by being stirred overnight and then spin-coated on the active layer at 3000 rpm for 40 s. Other conditions are the same as PM6:N3 based devices. The J – V curves of devices were measured under AM 1.5 G illumination with 100 mW cm $^{-2}$ by Keithley 2400 source meter and AAA solar simulator supplied by EnliTech (Taiwan). The EQE curves were obtained by the QE-R measurement system (EnliTech, Taiwan).

Microstructure and Mechanical Characterizations: The samples for GIWAXS measurements were prepared on pure silicon substrates and the conditions were the same as the device preparation. GIWAXS data of blend films were mainly acquired at beamline BL14B1 of Shanghai Synchrotron Radiation Facility (SSRF). The X-ray energy was 10 keV, corresponding to the wavelength of 1.24 Å. The incidence angle was 0.15° and the sample-to-detector distance was 357 mm by careful calibration.

The surface topography of films was measured by AFM (Bruker Multimode 8) in tapping mode. The type of AFM cantilever is RTESPA-300 with a k constant of about 40 N m $^{-1}$. The scanning area was 2 μ m \times 2 μ m and the scan rate is 1 Hz. The height images and phase images were obtained at the same time. The TEM images of films were obtained by a JEOL JEM-2100PLUS electron microscope and its accelerating voltage is 200 kV. The magnification of all TEM images is 30k. Infrared nanoimaging (IRs-SNOM) was conducted on an infrared scattering-type scanning near-field optical microscope (neaSNOM, Neaspec GmbH, Germany). Measurements are conducted in tapping mode. The images of topography, mechanical phase, optical amplitude of reflectivity, and optical phase of absorption were obtained at the same time. FTIR spectroscopy was performed with the IRTTracer-100 (Shimadzu Corporation). The details of FOE characterizations and PFQNM measurements could be found in a prior publication.^[28] The images of DMT modulus, adhesion, and deformation were obtained at the same time.

Supporting Information

Supporting Information is available from the Wiley Online Library or from the author.

Acknowledgements

L.Y. gratefully acknowledges the National Science Foundation of China (No. 52073207), the start-up grant of Peiyang Scholar program from Tianjin University, and the State Key Laboratory of Applied Optics (No. SKLAO2021001A17) for support. This work was also supported by the National Key Research and Development Program of China (Grant No. 2019YFA0705900) funded by MOST and the Basic and Applied Basic Research Major Program of Guangdong Province (Grant No. 2019B030302007). J.H. acknowledges the support from the National Natural Science Foundation of China (Nos. 21835006, 51961135103, and 51961165102). GIWAXS data were mainly acquired at Shanghai Synchrotron Radiation Facility (SSRF), beamline BL14B1. Part of the GIWAXS data acquisition was also carried out at SSRF, beamline BL16B1 and Beijing Synchrotron Radiation Facility (BSRF), beamline 1W1A. The authors greatly appreciate Dr. Xi Lu for his technical support on IR s-SNOM measurements and Asahi Kasei Corporation for supplying the SEBS materials.

Conflict of Interest

The authors declare no conflict of interest.

Author Contributions

L.Y. was in charge of this scientific research, conceived the idea, and designed the experimental protocols. Z.P. performed the mechanical and morphological measurements. K.X. and Z.P. performed the device fabrication and characterization. Q.Q. and Y.B.C. assisted the mechanical experiments. Y.C., Y.X., and J.H. supplied the high-efficiency photovoltaic materials. Z.P. performed the GIWAXS data acquisition. C.Y. acquired part of the GIWAXS data. L.Y. and Z.P. analyzed the data and drafted the paper with the help of Y.G., J.H., and J.L. All authors reviewed and edited the paper.

Data Availability Statement

The data that support the findings of this study are available from the corresponding author upon reasonable request.

Keywords

film morphology, mechanical properties, nonfullerene small molecule acceptors, organic solar cells, thermoplastic elastomers

Received: August 26, 2021

Revised: September 17, 2021

Published online: October 11, 2021

- [1] Y. Li, X. Guo, Z. Peng, B. Qu, H. Yan, H. Ade, M. Zhang, S. R. Forrest, *Proc. Natl. Acad. Sci. USA* **2020**, *117*, 21147.
- [2] P. Cheng, G. Li, X. Zhan, Y. Yang, *Nat. Photonics* **2018**, *12*, 131.
- [3] J. Yuan, H. Zhang, R. Zhang, Y. Wang, J. Hou, M. Leclerc, X. Zhan, F. Huang, F. Gao, Y. Zou, Y. Li, *Chem* **2020**, *6*, 2147.
- [4] D. J. Lipomi, *Joule* **2018**, *2*, 195.
- [5] Y. Ma, M. Zhang, S. Wan, P. Yin, P. Wang, D. Cai, F. Liu, Q. Zheng, *Joule* **2021**, *5*, 197.
- [6] Q. An, F. Zhang, J. Zhang, W. Tang, Z. Deng, B. Hu, *Energy Environ. Sci.* **2016**, *9*, 281.
- [7] J. Yao, B. Qiu, Z.-G. Zhang, L. Xue, R. Wang, C. Zhang, S. Chen, Q. Zhou, C. Sun, C. Yang, M. Xiao, L. Meng, Y. Li, *Nat. Commun.* **2020**, *11*, 2726.
- [8] Z.-G. Zhang, Y. Li, *Angew. Chem., Int. Ed.* **2021**, *60*, 4422.
- [9] X. Meng, L. Zhang, Y. Xie, X. Hu, Z. Xing, Z. Huang, C. Liu, L. Tan, W. Zhou, Y. Sun, W. Ma, Y. Chen, *Adv. Mater.* **2019**, *31*, 1903649.
- [10] Z. Hu, J. Wang, X. Ma, J. Gao, C. Xu, K. Yang, Z. Wang, J. Zhang, F. Zhang, *Nano Energy* **2020**, *78*, 105376.
- [11] L. Tan, Y. Wang, J. Zhang, S. Xiao, H. Zhou, Y. Li, Y. Chen, Y. Li, *Adv. Sci.* **2019**, *6*, 1801180.
- [12] C. Yan, S. Barlow, Z. Wang, H. Yan, A. K. Y. Jen, S. R. Marder, X. Zhan, *Nat. Rev. Mater.* **2018**, *3*, 18003.
- [13] J. Hou, O. Inganäs, R. H. Friend, F. Gao, *Nat. Mater.* **2018**, *17*, 119.
- [14] J. Zhang, H. S. Tan, X. Guo, A. Facchetti, H. Yan, *Nat. Energy* **2018**, *3*, 720.
- [15] P. Yin, Z. Yin, Y. Ma, Q. Zheng, *Energy Environ. Sci.* **2020**, *13*, 5177.
- [16] J. Xiong, J. Xu, Y. Jiang, Z. Xiao, Q. Bao, F. Hao, Y. Feng, B. Zhang, Z. Jin, L. Ding, *Sci. Bull.* **2020**, *65*, 1792.
- [17] M. Zhang, L. Zhu, G. Zhou, T. Hao, C. Qiu, Z. Zhao, Q. Hu, B. W. Larson, H. Zhu, Z. Ma, Z. Tang, W. Feng, Y. Zhang, T. P. Russell, F. Liu, *Nat. Commun.* **2021**, *12*, 309.
- [18] L. Zhan, S. Li, X. Xia, Y. Li, X. Lu, L. Zuo, M. Shi, H. Chen, *Adv. Mater.* **2021**, *33*, 2007231.
- [19] Y. Lin, Y. Firdaus, F. H. Isikgor, M. I. Nugraha, E. Yengel, G. T. Harrison, R. Hallani, A. El-Labban, H. Faber, C. Ma, X. Zheng,

- A. Subbiah, C. T. Howells, O. M. Bakr, I. McCulloch, S. D. Wolf, L. Tsetseris, T. D. Anthopoulos, *ACS Energy Lett.* **2020**, *5*, 2935.
- [20] P. Bi, S. Zhang, Z. Chen, Y. Xu, Y. Cui, T. Zhang, J. Ren, J. Qin, L. Hong, X. Hao, J. Hou, *Joule* **2021**, *5*, 2408.
- [21] Z. Chen, W. Song, K. Yu, J. Ge, J. Zhang, L. Xie, R. Peng, Z. Ge, *Joule* **2021**, *5*, 2395.
- [22] C. Li, J. Zhou, J. Song, J. Xu, H. Zhang, X. Zhang, J. Guo, L. Zhu, D. Wei, G. Han, J. Min, Y. Zhang, Z. Xie, Y. Yi, H. Yan, F. Gao, F. Liu, Y. Sun, *Nat. Energy* **2021**, *6*, 605.
- [23] W. Song, K. Yu, E. Zhou, L. Xie, L. Hong, J. Ge, J. Zhang, X. Zhang, R. Peng, Z. Ge, *Adv. Funct. Mater.* **2021**, *31*, 2102694.
- [24] F. Liu, L. Zhou, W. Liu, Z. Zhou, Q. Yue, W. Zheng, R. Sun, W. Liu, S. Xu, H. Fan, L. Feng, Y. Yi, W. Zhang, X. Zhu, *Adv. Mater.* **2021**, *33*, 2100830.
- [25] D. Rodriguez, S. Savagatrup, E. Valle, C. M. Proctor, C. McDowell, G. C. Bazan, T.-Q. Nguyen, D. J. Lipomi, *ACS Appl. Mater. Interfaces* **2016**, *8*, 11649.
- [26] J. Choi, W. Kim, S. Kim, T.-S. Kim, B. J. Kim, *Chem. Mater.* **2019**, *31*, 9057.
- [27] Q. Fan, W. Su, S. Chen, W. Kim, X. Chen, B. Lee, T. Liu, U. A. Méndez-Romero, R. Ma, T. Yang, W. Zhuang, Y. Li, Y. Li, T.-S. Kim, L. Hou, C. Yang, H. Yan, D. Yu, E. Wang, *Joule* **2020**, *4*, 658.
- [28] S. E. Root, S. Savagatrup, A. D. Printz, D. Rodriguez, D. J. Lipomi, *Chem. Rev.* **2017**, *117*, 6467.
- [29] N. Balar, Y. Xiong, L. Ye, S. Li, D. Nevola, D. B. Dougherty, J. Hou, H. Ade, B. T. O'Connor, *ACS Appl. Mater. Interfaces* **2017**, *9*, 43886.
- [30] W. Kim, J. Choi, J.-H. Kim, T. Kim, C. Lee, S. Lee, M. Kim, B. J. Kim, T.-S. Kim, *Chem. Mater.* **2018**, *30*, 2102.
- [31] Z. Peng, K. Jiang, Y. Qin, M. Li, N. Balar, B. T. O'Connor, H. Ade, L. Ye, Y. Geng, *Adv. Energy Mater.* **2021**, *11*, 2003506.
- [32] D. J. Lipomi, B. C.-K. Tee, M. Vosgueritchian, Z. Bao, *Adv. Mater.* **2011**, *23*, 1771.
- [33] D. J. Lipomi, H. Chong, M. Vosgueritchian, J. Mei, Z. Bao, *Sol. Energy Mater. Sol. Cells* **2012**, *107*, 355.
- [34] J. Han, F. Bao, D. Huang, X. Wang, C. Yang, R. Yang, X. Jian, J. Wang, X. Bao, J. Chu, *Adv. Funct. Mater.* **2020**, *30*, 2003654.
- [35] G.-U. Kim, Y. W. Lee, B. S. Ma, J. Kim, J. S. Park, S. Lee, T. L. Nguyen, M. Song, T.-S. Kim, H. Y. Woo, B. J. Kim, *J. Mater. Chem. A* **2020**, *8*, 13522.
- [36] Y. Lin, J. Wang, Z.-G. Zhang, H. Bai, Y. Li, D. Zhu, X. Zhan, *Adv. Mater.* **2015**, *27*, 1170.
- [37] K. Jiang, Q. Wei, J. Y. L. Lai, Z. Peng, H. K. Kim, J. Yuan, L. Ye, H. Ade, Y. Zou, H. Yan, *Joule* **2019**, *3*, 3020.
- [38] L. Arunagiri, Z. Peng, X. Zou, H. Yu, G. Zhang, Z. Wang, J. Y. Lin, J. Zhang, Y. Zheng, C. Cui, F. Huang, Y. Zou, K. S. Wong, P. C. Y. Chow, H. Ade, H. Yan, *Joule* **2020**, *4*, 1790.
- [39] Y. Qin, Y. Xu, Z. Peng, J. Hou, H. Ade, *Adv. Funct. Mater.* **2020**, *30*, 2005011.
- [40] K. Jiang, J. Zhang, Z. Peng, F. Lin, S. Wu, Z. Li, Y. Chen, H. Yan, H. Ade, Z. Zhu, A. K. Y. Jen, *Nat. Commun.* **2021**, *12*, 468.
- [41] Y. Cui, H. Yao, J. Zhang, K. Xian, T. Zhang, L. Hong, Y. Wang, Y. Xu, K. Ma, C. An, C. He, Z. Wei, F. Gao, J. Hou, *Adv. Mater.* **2020**, *32*, 1908205.
- [42] J. Yuan, Y. Zhang, L. Zhou, G. Zhang, H.-L. Yip, T.-K. Lau, X. Lu, C. Zhu, H. Peng, P. A. Johnson, M. Leclerc, Y. Cao, J. Ulanski, Y. Li, Y. Zou, *Joule* **2019**, *3*, 1140.
- [43] Y. Cui, H. Yao, J. Zhang, T. Zhang, Y. Wang, L. Hong, K. Xian, B. Xu, S. Zhang, J. Peng, Z. Wei, F. Gao, J. Hou, *Nat. Commun.* **2019**, *10*, 2515.
- [44] Z. Luo, R. Ma, T. Liu, J. Yu, Y. Xiao, R. Sun, G. Xie, J. Yuan, Y. Chen, K. Chen, G. Chai, H. Sun, J. Min, J. Zhang, Y. Zou, C. Yang, X. Lu, F. Gao, H. Yan, *Joule* **2020**, *4*, 1236.
- [45] R. Ma, T. Liu, Z. Luo, Q. Guo, Y. Xiao, Y. Chen, X. Li, S. Luo, X. Lu, M. Zhang, *Sci. China: Chem.* **2020**, *63*, 325.
- [46] Y. Cui, Y. Xu, H. Yao, P. Bi, L. Hong, J. Zhang, Y. Zu, T. Zhang, J. Qin, J. Ren, Z. Chen, C. He, X. Hao, Z. Wei, J. Hou, *Adv. Mater.* **2021**, 2102420, <https://doi.org/10.1002/adma.202102420>.
- [47] S. Tang, Y. Xu, G. Su, J. Bao, A. Zhang, *RSC Adv.* **2018**, *8*, 35429.
- [48] B. Roth, S. Savagatrup, N. V. de los Santos, O. Hagemann, J. E. Carlé, M. Helgesen, F. Livi, E. Bundgaard, R. R. Søndergaard, F. C. Krebs, D. J. Lipomi, *Chem. Mater.* **2016**, *28*, 2363.
- [49] D. Pei, Z. Wang, Z. Peng, J. Zhang, Y. Deng, Y. Han, L. Ye, Y. Geng, *Macromolecules* **2020**, *53*, 4490.
- [50] B. O'Connor, E. P. Chan, C. Chan, B. R. Conrad, L. J. Richter, R. J. Kline, M. Heeney, I. McCulloch, C. L. Soles, D. M. DeLongchamp, *ACS Nano* **2010**, *4*, 7538.
- [51] J. Y. Chung, A. J. Nolte, C. M. Stafford, *Adv. Mater.* **2011**, *23*, 349.
- [52] O. Awartani, B. I. Lemanski, H. W. Ro, L. J. Richter, D. M. DeLongchamp, B. T. O'Connor, *Adv. Energy Mater.* **2013**, *3*, 399.
- [53] D. E. Martínez-Tong, A. S. Najar, M. Soccio, A. Nogales, N. Bitinis, M. A. López-Manchado, T. A. Ezquerro, *Compos. Sci. Technol.* **2014**, *104*, 34.
- [54] H. Gao, K. Youssef, L. Li, X. Zhu, Q. Pei, *J. Polym. Sci., Part B: Polym. Phys.* **2018**, *56*, 814.
- [55] D. Wang, K. Nakajima, F. Liu, S. Shi, T. P. Russell, *ACS Nano* **2017**, *11*, 8660.
- [56] S. Kim, J.-H. Kim, J.-G. Oh, K.-L. Jang, B.-H. Jeong, B. K. Hong, T.-S. Kim, *ACS Appl. Mater. Interfaces* **2016**, *8*, 15391.
- [57] J.-H. Kim, A. Nizami, Y. Hwangbo, B. Jang, H.-J. Lee, C.-S. Woo, S. Hyun, T.-S. Kim, *Nat. Commun.* **2013**, *4*, 2520.
- [58] D. Rodriguez, J.-H. Kim, S. E. Root, Z. Fei, P. Boufflet, M. Heeney, T.-S. Kim, D. J. Lipomi, *ACS Appl. Mater. Interfaces* **2017**, *9*, 8855.
- [59] L. Ye, X. Jiao, M. Zhou, S. Zhang, H. Yao, W. Zhao, A. Xia, H. Ade, J. Hou, *Adv. Mater.* **2015**, *27*, 6046.
- [60] S. Mukherjee, X. Jiao, H. Ade, *Adv. Energy Mater.* **2016**, *6*, 1600699.
- [61] M. Schubert, D. Dolfen, J. Frisch, S. Roland, R. Steyrleuthner, B. Stiller, Z. Chen, U. Scherf, N. Koch, A. Facchetti, D. Neher, *Adv. Energy Mater.* **2012**, *2*, 369.
- [62] S. H. Park, S. Park, S. Lee, J. Kim, H. Ahn, B. J. Kim, B. Chae, H. J. Son, *Nano Energy* **2020**, *77*, 105147.
- [63] Y.-C. Huang, Y.-C. Liao, S.-S. Li, M.-C. Wu, C.-W. Chen, W.-F. Su, *Sol. Energy Mater. Sol. Cells* **2009**, *93*, 888.
- [64] C. Westermeier, A. Cernescu, S. Amarie, C. Liewald, F. Keilmann, B. Nickel, *Nat. Commun.* **2014**, *5*, 4101.
- [65] M. Goikoetxea, I. Amenabar, S. Chimenti, M. Paulis, J. R. Leiza, R. Hillenbrand, *Macromolecules* **2021**, *54*, 995.
- [66] W. Ma, C. Yang, A. J. Heeger, *Adv. Mater.* **2007**, *19*, 1387.
- [67] R. Alessandri, J. J. Uusitalo, A. H. de Vries, R. W. A. Havenith, S. J. Marrink, *J. Am. Chem. Soc.* **2017**, *139*, 3697.
- [68] A. G. Facca, M. T. Kortschot, N. Yan, *Composites, Part A* **2006**, *37*, 1660.
- [69] A. Y. Coran, R. Patel, *J. Appl. Polym. Sci.* **1976**, *20*, 3005.
- [70] W. Voigt, *Ann. Phys.* **1889**, *274*, 573.
- [71] A. Reuss, *Z. Angew. Math. Mech.* **1929**, *9*, 49.
- [72] A. Y. Coran, R. Patel, *Rubber Chem. Technol.* **1981**, *54*, 91.
- [73] W. Zhao, D. Qian, S. Zhang, S. Li, O. Inganäs, F. Gao, J. Hou, *Adv. Mater.* **2016**, *28*, 4734.
- [74] J.-W. Lee, B. S. Ma, J. Choi, J. Lee, S. Lee, K. Liao, W. Lee, T.-S. Kim, B. J. Kim, *Chem. Mater.* **2020**, *32*, 582.
- [75] B. Zhao, O. Awartani, B. O'Connor, M. A. Zikry, *J. Polym. Sci., Part B: Polym. Phys.* **2016**, *54*, 896.
- [76] S. Y. Son, J.-H. Kim, E. Song, K. Choi, J. Lee, K. Cho, T.-S. Kim, T. Park, *Macromolecules* **2018**, *51*, 2572.
- [77] J. Liu, M. Gao, J. Kim, Z. Zhou, D. S. Chung, H. Yin, L. Ye, *Mater. Today* **2021**, <https://doi.org/10.1016/j.mattod.2021.08.004>.